https://doi.org/10.1016/j.cemconcomp.2022.104443

Corrosion Behavior of Carbon Steel in Chloride-Contaminated Ultra-High-Performance Cement Pastes

Haibing Zheng [a, b], Jianxin Lu [b], Peiliang Shen [b], Li Sun [a], Chi Sun Poon [b, *], Weihua Li [a, *]

a College of Chemical Engineering and Technology, Sun Yat-sen University, Tangjiawan, Zhuhai, 519082, China

b Department of Civil and Environmental Engineering, The Hong Kong Polytechnic University, Hong Kong

***Corresponding authors:**

Chi Sun Poon, E-mail: cecspoon@polyu.edu.hk

Weihua Li, E-mail: liweihua3@mail.sysu.edu.cn

Abstract:

In this work, the corrosion behavior of carbon steels embedded in normal-performance cement pastes (NPCP) and ultra-high-performance cement pastes (UHPC) contaminated with seawater were studied. The results showed that the corrosion of the carbon steel propagated in NPCP due to the relatively low resistivity of the matrix. The initial high Cl^-/OH^- ratio induced the corrosion of steel after the cast of the seawater mixed UHPC, however it was suppressed immediately within the first few days due to the significant reduction of water, which inhibited the anodic reaction of the corrosion process. The insufficient oxygen supply did not dominate the corrosion process, since the phase conversion of the corrosion products could also sustain the cathodic reaction.

Keywords:

Ultra-high-performance concrete; Carbon steel; Seawater; Chloride ion; Corrosion

1. Introduction

Corrosion of steel bars is one of the main causes for the durability problem of reinforced concrete structures in marine environment. Generally, hardened concrete has an internal porous cementitious matrix which is filled with an alkaline pore solution [1-3]. The corrosion behavior of the embedded steel is highly related to this porous cement matrix [4-10]. For a high-quality dense concrete, the corrosion risk is usually much lower, and it will increase the chloride penetrating path and delay the corrosion initiation during the service life of structures [11]. With the advance of concrete technology, ultra-high-performance concrete has been developed and applied in practice for over two decades.

Ultra-high-performance concrete is a kind of innovative cementitious material exhibiting very high strength and exceptional good durability, which is normally prepared with extremely low w/c ratios based on the principle of compact packing [12-16]. It exhibits high particle packing density and thus can be defined as a dense concrete. Due to the superior durability, it was recognized as an excellent candidate for

infrastructures with long service life in aggressive environment. The low w/b ratio and low porosity of such kind of concrete result in significant lower water, gas and chloride permeability. The water absorption coefficient of ultra-high-performance concrete was five times lower than conventional concrete [17]. The gas permeability coefficient, generally lower than 1.0×10^{-19}, was found to be three magnitude lower than the conventional concrete [18]. The chloride diffusion efficient was at least one magnitude lower compared with high performance concrete, which was ranged from 0.2×10^{-13} m^2/s to 4.1×10^{-13} m^2/s depending on the w/b ratio. With high durability, the corrosion rate of steel bar in ultra-high-performance concrete was reported to be around $0.01\mu A/cm^2$ after 1 year of immersion in 3.5% NaCl solution, and no chloride was detected at the steel bar, indicating no corrosion occurred [19]. The corrosion initiation was significantly postponed under accelerated corrosion test [20]. El-Joukhadar [21] investigated the corrosion behavior of steel bar in Ultra High Performance Fiber Reinforced Concrete (UHPFRC) by applying a constant voltage to accelerate corrosion. It was also found that the corrosion was fully mitigated by UHPFRC without service cracks, but the effectiveness decreased with the increase of the crack width. In the previous studies, the corrosion behavior induced by external aggressive ions are investigated, and the studies on the corrosion-mechanism of steel bar in such dense cementitious materials are still limited. In addition, the corrosion behavior of steel bar in chloride-contaminated ultra-high-performance concrete is rarely studied, which is critical for the knowledge of the corrosion resistance of such innovative cementitious materials. The endogenous chloride usually originates from the binding materials, mixing water or sea-dredged aggregates [22].

For chloride contaminated concrete, Cl^-/OH^- ratio in the concrete pore solution was recognized as a critical parameter for the corrosion initiation of steel bars [23-26]. The steel bar could not be passivated when this ratio is higher than the critical value (0.66~1.4 [24]). With the progress of cement hydration, a part of the chloride ions could be chemically bounded to the hydrates. For example, Friedel's salt could be formed with the presence of C_3A in cement, and chloroferrite phase, which is analogous to Friedel's salt, could also be formed in cement with a low content of C_3A due to the additional physical absorption

by C-S-H [27]. Thus, the content of free chloride in the pore solution can be reduced with the progress of hydration of cement. Simultaneously, the water in the pore solution would also be consumed continuously. As a consequence, the corrosive internal environment keeps varying during the early age of the cement hydration. For ultra-high-performance concrete, the water to binder ratio and the hydration degree of cement are both much lower than that of the normal performance concrete, and the microstructure are extremely dense. The changes of the corrosive environment with time and its effects on the corrosion behavior of chloride-contaminated ultra-high-performance concrete is still not clear.

The aim of this work is to study the initial corrosion behavior of carbon steel in chloride-contaminated ultra-high-performance concrete, revealing the corrosion mechanism. To achieve this, the chemistry of the pore solution and microstructure of the cement pastes were firstly evaluated to characterize the internal environments for the steel corrosion. Then, the corrosion behavior was monitored by using electrochemical test methods, including open circuit potential (OCP) and electrochemical impedance spectroscopy (EIS). The resistivity of the concrete, which is one of the critical factors was also analyzed. The passive film formed on the steel was characterized by using X-ray photoelectron spectroscopy (XPS). The surface morphology of the carbon steel with corrosion products was characterized by using scanning electron microscopy (SEM) and energy-dispersive X-ray spectroscopy (EDS).

2. Experimental program

2.1. Materials and sample preparation

The Green Island Portland Cement (CEM I 52.5, BS EN1971:2000) produced in Hong Kong was used. The silica fume (powder form) used in the present work was supplied by a company in mainland China. The compositions of the cement and silica fume obtained by XRF (Rigaku Supermini200) are shown in **Table 1**. A polycarboxylic ether (PCE) based superplasticizer (MasterGlenium ACE 8588) was used to prepare the cement pastes. The mix proportions of cement pastes are shown in **Table 2**. Cement pastes with a water to binder (w/b) ratio of 0.4 was prepared to simulate the normal-performance concrete,

which is denoted as NPCP. Silica fume is a critical component in preparing UHPC, and 20% silica fume by weight of binder was used in this work [28, 29]. A w/b ratio of 0.143 was designed to represent an ultra-high-performance concrete, which was denoted as UHPC. Seawater is a typical chloride resource for the corrosion initiation of steel bar in concrete. It is generally known that seawater mixed concrete is an extremely corrosive environment for the embedded steel bars. Corrosion of steel bar occurs immediately after the cast of the normal performance concrete mixed with seawater [11, 30, 31]. To simulate a severely chloride-contaminated condition, seawater was used as mixing water to prepare the cement pastes in this work. It was prepared according to ASTM D1141 [32]: NaCl, $MgCl_2$, Na_2SO_4, $CaCl_2$, KCl and $NaHCO_3$ and the calculated Cl^- concentration was 0.558 M. The constitutes of the NPCPs were first mixed with a low speed for 1 min and further mixed for 2 min at a high speed. For the UHPCs, the binder materials were first dry mixed for 5 min to fully disperse the silica fume added. After the addition of water/seawater, it was then low speed mixed for 2 min and high-speed mixed for 5 min, and then low speed mixed again for 2 min to remove the entrapped air voids during the high-speed mixing procedure.

The steel specimens were prepared from the S275J0 (EN 100252: 2004) carbon steel. The chemical composition of the steel provided by the manufacturer is shown in **Table 3**. A copper wire was soldered to one end of the sample for electric connection. It was sealed with an epoxy resin leaving an exposed area of 0.856 ± 0.02 cm^2 and then grinded successively from Grit 180 to 600 with emery papers. The steel specimens were then fixed in moulds with a size of $40 \times 40 \times 40$ mm designed with a cement paste cover depth of 10 mm. The cement pastes were cast carefully into the mould with manual vibration to remove air bubbles ensuring good contacts with the steel surface. The detailed information of the steel specimens were shown in the previous work [33]. In parallel, cement paste specimens ($40 \times 40 \times 40$ mm) without steel were prepared for the characterization of the internal environment. Three parallel specimens were prepared for each group. Thus, 12 cement paste specimens with steel and 12 cement paste specimens without steel were prepared respectively. All the specimens were demoulded after 24 h and cured in an environmental chamber with a temperature of 22 ± 1 °C and a relative humidity of 90%.

Table 1 Oxide compositions of binders (% w/w)

Material	MgO	Al_2O_3	SiO_2	CaO	TiO_2	Fe_2O_3	SO_3	MnO	K_2O
Cement	1.47	3.77	19.37	63.85	0.26	3.08	5.38	0.06	0.69
Silica Fume	0.90	0.40	91.00	1.00	—	1.80	0.18	—	1.70

Table 2 Mix proportions and CH content of cement pastes.

Mix	w/b	Mixing water	Cement (%)	SF (%)	SP (%)	CH content (%)	Porosity (%)
DW-NPCP	0.4	DI water	100	—	—	14.02	18.57
SW-NPCP	0.4	Seawater	100	—	—	14.92	17.77
DW-UHPC	0.143	DI water	80	20	0.8	2.56	4.60
SW-UHPC	0.143	Seawater	80	20	0.8	2.61	5.36

Note: w/b: water to binder ratio, SF: silica fume, SP: superplasticizer, CH: $Ca(OH)_2$. CH content in wt.% of cement paste was calculated according to the TG analysis as reported in [34].

Table 3 Chemical compositions of carbon steel (% w/w).

C	Mn	P	S	Si	Al	Nb	Cr	Ni	Mo	Cu
0.18	0.8	0.011	0.007	0.20	0.031	0.001	0.02	0.011	0.001	0.005

2.2. Test methods

2.2.1 Internal environment of cement paste

The corrosion behavior of steel was governed by many properties of the internal environment of the concrete, such as the pH of the pore solution, the concentrations of aggressive ions, the availability of oxygen, temperature, internal humidity, the resistivity and the characteristics of the steel/concrete interface [4, 35]. In the present work, the chemistry and pore structure of cement paste were monitored to assist the analysis of the corrosion behavior of carbon steel.

Pore water expression (PWE) is a popular and the most reliable method to study the pore solution chemistry [36-39]. Attempts were made to obtain the pore solutions of the UHPC by the PWE method after 1 d but failed. This was attributed to the low water to cement ratio, low porosity and very low internal humidity (self-desiccation) of UHPC [40-42].

As such, for the first few hours before the initial set of the cement paste, the pore solutions were extracted by a 10,000-rpm centrifugation with for 5 min. After the setting of the cement paste, the pore solution was extracted by PWE method using a pore solution expression device. The pH values of the pore solutions were tested directly after the filtration using a REX PHS-3C pH meter. The concentrations of the chloride and calcium ions in the pore solutions were tested by using a Mettler Toledo EasyPlus Titrator Easy CI and a Cole-Parmer Model 360 Flame Photometer respectively.

The free and total chloride contents in cement pastes was quantified by using a washing method after 56 d curing. Due to the presence of a large amount of un-hydrated particles in UHPC, the time of washing should be as short as possible to avoid the rehydration of these particles. Considering this, the cement pastes were crushed and grounded to a particle size < 315μm [43]. For the free chloride test, 5 g sample was added into 200 mL deionized water and agitated for 3 min at room temperature. The resulting solution was filtered immediately and stabilized using 2 mL nitric acid (53%). For the total chloride test, 5 g sample was added into 50 mL deionized water agitating for 2 min, and the nitric acid prepared with 80 mL water + 20 mL 53% nitric acid solution was added and continued agitating for 30 min. Then the solution was filtered, and the chloride content was measured using the potential titration method as mentioned above.

After 56 d curing, the cement pastes were freeze-dried for 24 h and then grounded to particle sizes < 75 μm. X-ray diffraction (Rigaku UItima IV) patterns were recorded for the four groups of cement pastes. The data acquisition over the range of 5.0°- 70.0° 2θ with a step size of 0.02°. The pore structure of NPCP and UHPC was measured using Mercury Intrusion Porosimetry (MIP, Micromeritics AutoPore IV 9500 Series) after 28 days of curing.

2.2.2 Corrosion behavior monitoring

The corrosion behavior of carbon steel in cement pastes was characterized by electrochemical test methods (Multi-Autolab M 204 workstation). A three-electrode system was used, of which the reference

electrode was a saturated calomel electrode (SCE), the counter electrode was a stainless-steel plate. The counter electrode and reference electrode were connected through a wet sponge, facing the working electrode to ensure a good current distribution [33].

Open circuit potential (OCP) was tested periodically to assess the corrosion risk of the carbon steel. However, it has been known that the OCP of steel in a very dense matrix, such as UHPC, is influenced by the availability of gaseous oxygen. In the present work, the OCP results was discussed in the light of whether gaseous oxygen was present. Due to the high resistivity of the UHPC, the electrochemical impedance spectroscopy (EIS) was regarded as more suitable to detect the corrosion rate of the carbon steel when compared with linear polarization resistance (LPR) test [44]. As such, EIS test with a 10-mV sine perturbation was conducted after OCP became stable. The OCP was determined until the variation of the potential with time (dV/dt) was lower than 1 μV/s. A frequency range of 100 kHz ~ 10 mHz with seven points per frequency decade was used [45]. The software of Zsimpwin was used to simulate the EIS test results.

Finally, the paste specimens with steel were split open after 56 d of curing, and the steel samples were extracted for surface observations, by which the steel/paste interfaces and the morphologies of the corrosion products could be characterized. In order to remove the loose cement hydration products remained on the steel surface, the steel samples were immediately immersed into ethanol and cleaned in an ultrasonic device for 5 min. Then they were dried by using N_2 flow and stored in a plastic bag filled with N_2 gas before the surface characterization. To reveal the chemistry of the passive film formed, X-ray photoelectron spectroscopy (XPS) tests were conducted on the surface of the steel samples. An XPS spectrometer with an Al K α X-Ray source was used, the analytical chamber pressure was set as 2×10^{-9} Pa. The survey spectra and the high-resolution spectra of Fe 2p were recorded. The results were analyzed by using an Xpspeak software. Scanning Electron Microscopy (VEGA 3 TESCAN) with an Energy-dispersive X-ray spectroscopy (EDS) was used for the surface characterization of morphology on steel samples.

3. Results and Discussion

3.1 Internal environment monitoring

3.1.1 pH value and Ca^{2+} concentration in pore solution

It is well recognized that the OH^- ions in the pore solution acts as the "corrosion inhibitor" and promotes the passivation of the steel in concrete. In **Fig. 1**, the pH value of the pore solution in NPCPs increased significantly within 1 d and then increased further slightly with time. The pH values of pore solution of SW-NPCP were lower than those of DW-NPCP. For UHPCs, the overall pH values within 1 d were much higher than those of NPCPs. It has been reported in many researches [46-48] that the silica fume may act as inert diluent at the early age (within 1 d), which would accelerate the hydration of cement. By this, the content of the alkali in pore solution would be increased within 1 d, exhibiting higher pH values [46, 47]. Therefore, the higher pH value in UHPCs was most probably due to the dilution effect of silica fume. Higher cement to water ratio might also be an important cause for the higher pH value compared with NSCP [47]. More reactant (cement) will promote the hydration process. With the progress of cement hydration, the pH value would decrease to low level due to the pozzolanic reaction between the silica fume and the alkali in the pore solution [46, 47, 49]. Although the pH value of UHPCs after 1 d could not be obtained, it could be speculated that the pH value would reduce afterwards due to the pozzolanic reaction, which could consume a large amount of CH. This could also be reflected from the pH results obtained by leaching method as shown in **Table 4**. The pH values of SW-UHPC were lower than those of DW-UHPC. The reduction of pH values caused by the seawater can possibly be explained by the presence of high concentration of Ca^{2+} in seawater. The concentration of Ca^{2+} in the pore solution of SW-NPCP was much higher than those in DW-NPCP as shown in **Fig. 1** and the additional Ca^{2+} in seawater could break the solubility equilibrium of $Ca(OH)_2$ and result in decrease of the amount of dissolved $Ca(OH)_2$.

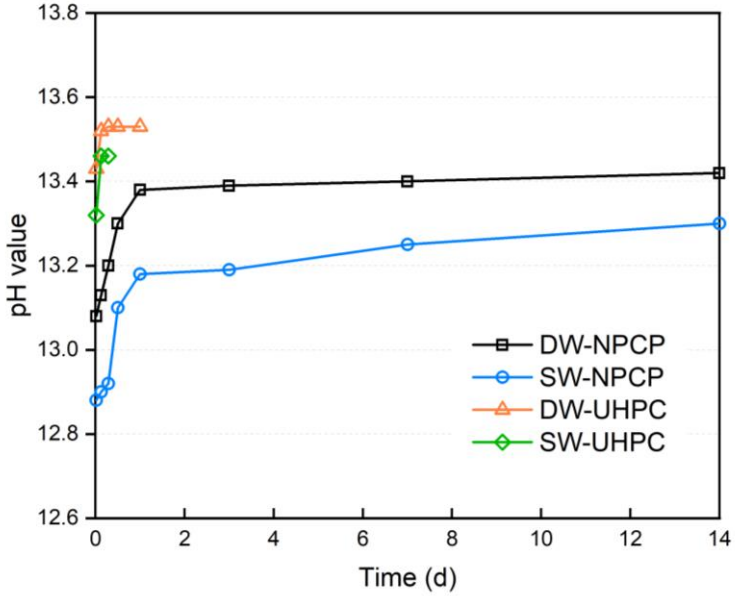

(a)

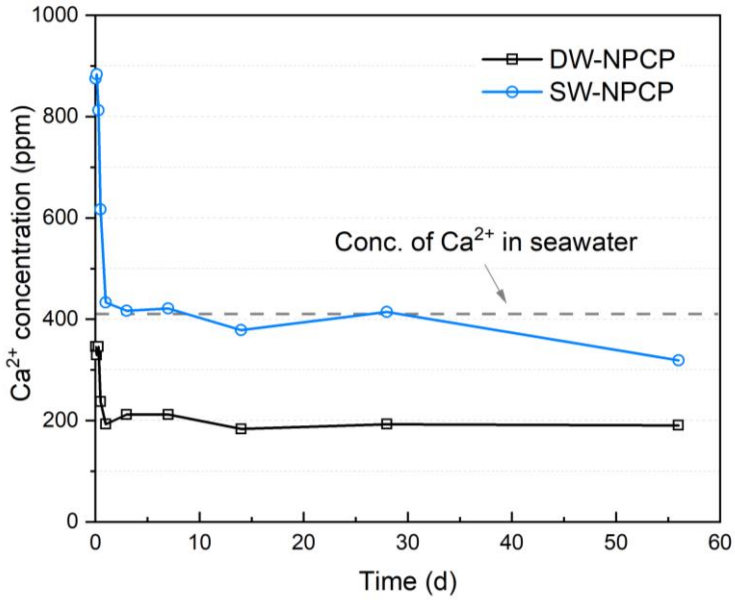

(b)

Fig. 1. Change of (a) pH value of pore solution and (b) concentrations of calcium ion with time.

3.1.2 Chloride in cement pastes

The concentration of the free chloride ion in the pore solution are presented in **Fig. 2(a)**. After the commencement of the cement hydration, the Cl^- concentration in SW-NPCP increased sharply to a very

high value around 0.7 M (much higher than that in seawater) after ca. 12 h, which is in agreement with the results in [50]. During the reaction of cement with seawater, water was consumed for the hydration of cement and simultaneously the Cl^- was chemically or physically absorbed during the hydration of cement. Compared with OH^-, the Cl^- in seawater could preferentially react with C_3A by intercalating the interlayers of $[Ca_2Al(OH)_6]^+$ to form Friedel's salt (**Equation (1)**) [51].

$$4Ca^{2+} + 2Al(OH)_4^- + 2Cl^- + 4OH^- + 4H_2O \rightarrow Ca_4Al_2Cl_2(OH)_{12}\cdot 4H_2O \text{ (Friedel's salt)} \quad (1)$$

Cl^- could also be physically absorbed by the hydration products C-S-H, forming the chloroferrite phase which is analogous to Friedel's salt [27]. The sharp increase of Cl^- concentration in SW-NPCP was mainly due to the quick consumption of water for the cement hydration. Such a high Cl^- concentration would increase the risk of corrosion of the steel in cement paste. The Cl^- concentration in SW-UHPC were much lower compared with SW-NPCP during the first several hours. As discussed above, the C_3A/Cl^- ratio is much higher in UHPCs, and the hydration rate of C_3A is much higher compared with the other clinkers. Therefore, higher proportion of Cl^- could be absorbed resulting in the significant reduction of Cl^- concentration in the pore solution. After 12 h, the Cl^- concentration in SW-NPCP decreased significantly, and it was attributed to the chemical and physical binding behavior of chloride by the hydration products of cement. As mentioned in previous work, very little Friedel's salt could be formed in seawater mixed concrete, the reduction of Cl^- was mainly due to the physical absorption of the C-S-H [50]. After 7 d, the decreasing rate of Cl^- concentration stabilized. This was due to the reduction of the hydration rate of cement. After 56 d, the Cl^- concentration dropped to a very low level of 0.23 M. This indicated that a large proportion of Cl^- was bound by the hydration products. As shown in the XRD patterns of the cement pastes of **Fig. 3**, Friedel's salt was detected in SW-NPCP but was not detected in SW-UHPC.

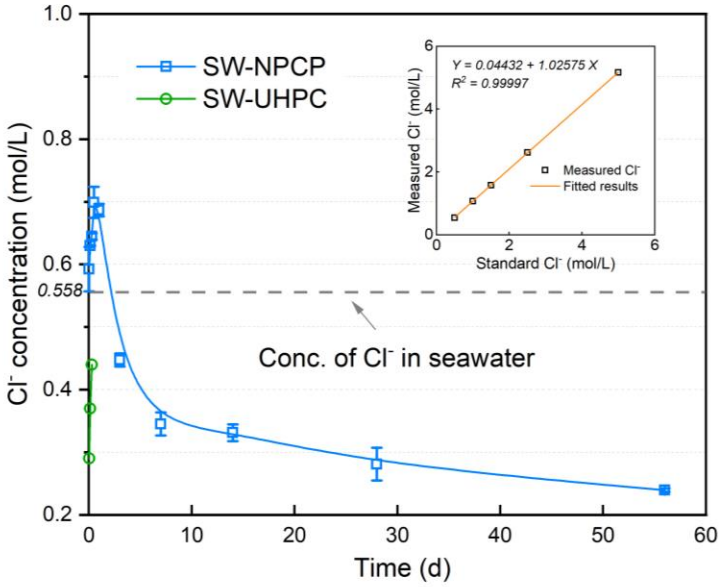

(a)

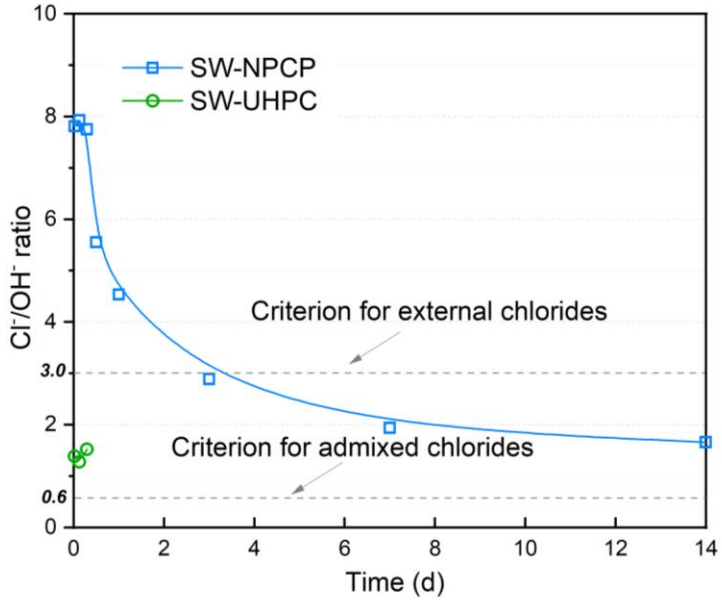

(b)

Fig. 2. Evolutions of (a) Cl^- concentration and (b) Cl^-/OH^- ratio in pore solutions of SW-NPCP and SW-UHPC.

To quantitatively evaluate the binding of Cl^- in the cement pastes, the free and total chloride contents were measured after 56 d as displayed in **Table 4**. It can be seen that only a small portion of chloride remained as free chloride in the cement paste, and a major part of chloride was chemically or physically

bound by the cement hydration products both in SW-NPCP and SW-UHPC. Similarly, it was reported that a large portion of the Cl^- was consumed to form the Friedel's salts in normal concrete [52, 53]. The free/total chloride ratio of SW-UHPC was much lower than those of SW-NPCP. The measured total chloride contents of the two groups of samples were both lower than the calculated chloride contents according to the mix proportion. This might be due to the leaching of ions during the curing process.

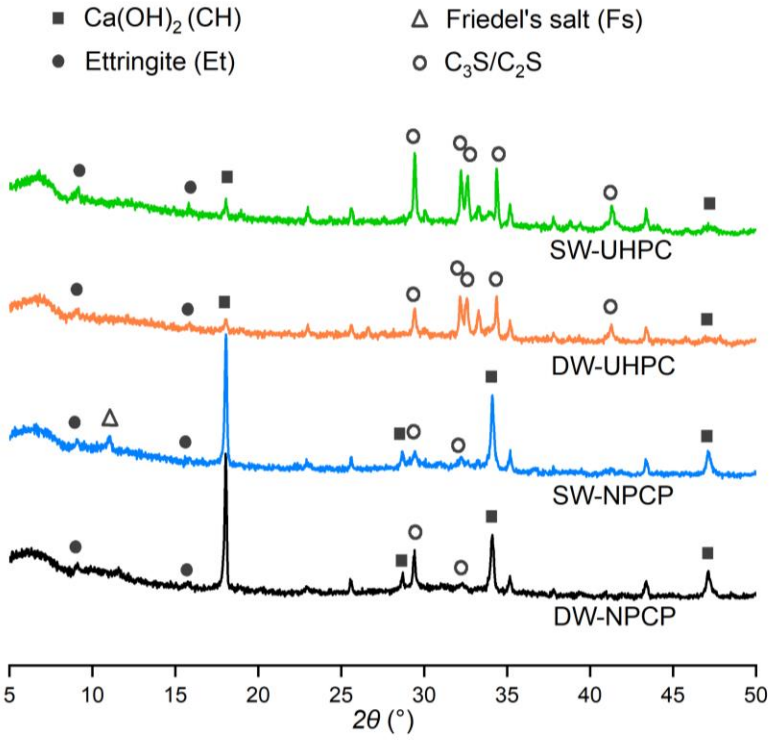

Fig. 3. XRD patterns of cement pastes

Table 4

Chloride content (by mass of cement paste) and pH value of leachate of seawater mixed cement pastes.

ID	Calculated chloride content (%) *	Measured chloride content (%)		Free/total chloride ratio	pH value
		Total chloride	Free chloride		
SW-NPCP	0.79	0.5452	0.0741	0.1359	12.29
SW-UHPC	0.28	0.1957	0.0149	0.0761	11.93

* Calculated chloride content was based on the mix proportion and composition of seawater.

In seawater, besides chloride ion, SO_4^{2-} has also been reported to be a potential aggressive ion for steel and exhibits negative effect on the corrosion of steel bars in concrete [54-57]. However, the concentration of SO_4^{2-} is much lower as compared with Cl^- and it can be readily consumed to form the ettringite at the very early age [30]. Therefore, Cl^- would dominate the corrosion process of the steel in the cement-based system. Hence, the influence of SO_4^{2-} on the steel corrosion was not considered in this work.

The corrosion of the steel bars in concrete is reported as the result of the competitive absorption of the aggressive ion Cl^- and the inhibiting ion OH^- on the iron atoms of the steel surface. Therefore, it was proposed that the Cl^-/OH^- mole ratio can be used to define the chloride threshold value of steel bars in concrete [24]. This ratio was also recognized as a critical criterion to predict the corrosion risk of the steel bars in concrete or simulated pore solutions with admixed chloride [23, 58]. To assess the corrosion risk of the carbon steel, the Cl^-/OH^- mole ratio was also determined, in which the concentration of OH^- was calculated from the measured pH values according to the following equation [37]:

$$pH = 14 + \log [OH^-] \quad (2)$$

As displayed in **Fig. 2(b)**, the Cl^-/OH^- ratio in SW-NPCP increased slightly during the first few hours and decreased exponentially with time. The criterions of Cl^-/OH^- ratio for the concrete/mortar admixed with chloride proposed by the researchers varied a lot as summarized in [59]. The initial Cl^-/OH^- ratio was high enough for the corrosion of the unpassivated carbon steel in the fresh cement paste according to the lower boundary of 0.6 proposed by Hausmanns [23, 24]. The decrease of this ratio with time indicated the reduction of the corrosivity of the pore solution, which was related to the corrosion rate of the actively corroding steel. For SW-UHPC, the initial Cl^-/OH^- ratio was significantly lower compared with SW-NPCP, but it was still higher than the corrosion criterion for the cases with admixed chlorides. The corrosion of steel in SW-UHPC was expected to occur at the beginning. The subsequent evolution of Cl^-/OH^- ratio in SW-UHPC could not be obtained due to the difficulty of extracting the pore solution.

3.1.3 Pore structure of cement paste

The porosities and the pore size distributions of cement pastes after 28 d are shown in **Table 2** and **Fig. 4** respectively. The critical pore diameter of SW-NPCP was shifted to the left and the peak value was lower compared with the DW-NPCP. The size and the amount of the capillary pores, which is the dominant factor determining the porosity, were reduced with the use of seawater, thus resulting in a lower porosity. It was mainly due to the accelerated hydration of cement caused by the ions present in seawater [52]. In addition, the volume of the gel pores with the size less than 10 nm increased significantly in the SW-NPCP, which is in agreement with the results in the previous studies [50, 60]. For the UHPCs, the porosity was much lower, and the critical pore diameter was reduced by nearly one order of magnitude compared to the DW-NPCP. Most of the pores in UHPCs were located at the region < 20 nm, which indicated an ultra-low permeability of the cement paste. Similarly, the volume of gel pores was increased in the SW-UHPC compared with DW-UHPC, which may be the dominant factor facilitating the increase of the porosity. The ultra-dense structures of the UHPCs would largely prevent the migration of internal and external ions in the matrix. On the one hand, the ingress of aggressive ions, e.g., Cl^-, CO_2 and SO_4^{2-}, would be difficult due to the ultra-low ion, gas and water permeability, increasing the durability of the concrete matrix. On the other hand, the electrochemical process of corrosion on steel bar would be difficult to proceed without the ion, water and gas exchange.

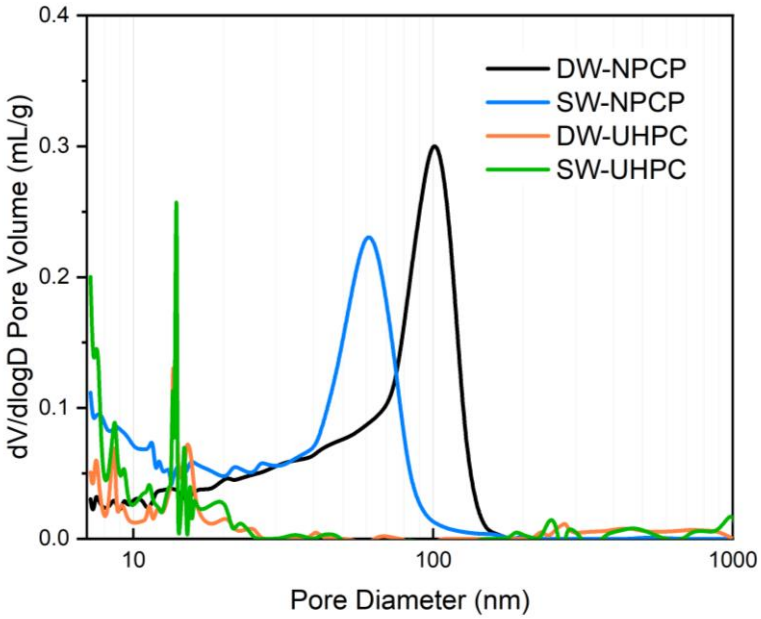

Fig. 4. Pore size distributions of cement pastes.

3.2. Corrosion behavior of carbon steel

3.2.1 Electrochemical impedance spectroscopy and resistivity of cement pastes

Fig. 5 displays the EIS test results of the carbon steel in different cement pastes. It is worth to note that the desired EIS signal of SW-UHPC specimens could not be obtained after 28 d, and the related results for this group of specimens were not recorded. Attempts had been done to select a proper equivalent circuit for the EIS analysis based on the physical meaning of the elements in the steel/paste interface and literature review [33, 61, 62]. Two time constants were needed to satisfy the analysis in the present work, even though they could not always be obviously observed in some plots due to the possible super-position. The EIS results were fitted using the equivalent circuit as shown in **Fig. 6**, which showed the best fitting parameter and low error. R_0 represents the paste resistance. R_1 and Q_1 respectively represent the resistance and capacitance of the passive film in DW-NPCP/UHPC or the corrosion products in SW-NPCP/UHPC. R_2 and Q_2 denote the charge transfer resistance and the double layer capacitance respectively [63]. The detailed fitting results of each parameter were shown in **Table 5** (the degree of deviation, $\chi^2 < 10^{-3}$).

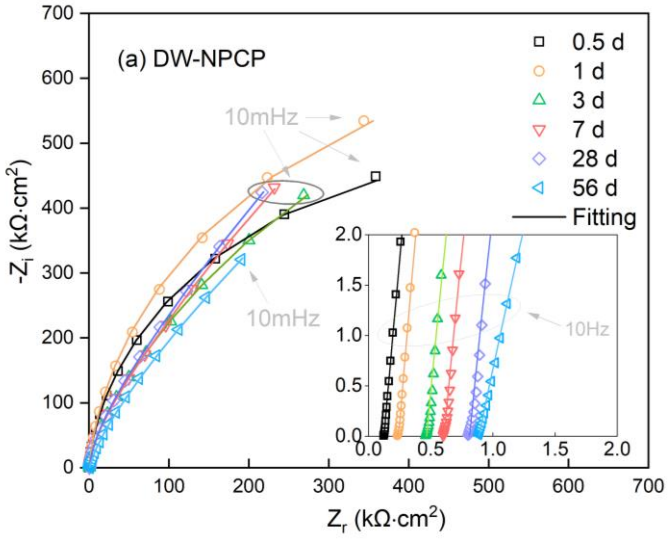
(a) DW-NPCP
0.5 d
1 d
3 d
7 d
28 d
56 d
Fitting
10mHz
10mHz
10Hz
-Z_i (kΩ·cm^2)
Z_r (kΩ·cm^2)

318

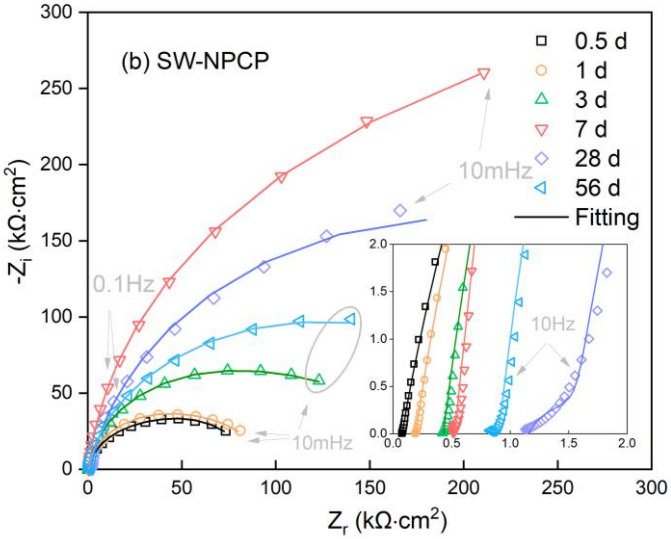
(b) SW-NPCP
0.5 d
1 d
3 d
7 d
28 d
56 d
Fitting
10mHz
0.1Hz
10mHz
10Hz
-Z_i (kΩ·cm^2)
Z_r (kΩ·cm^2)

319

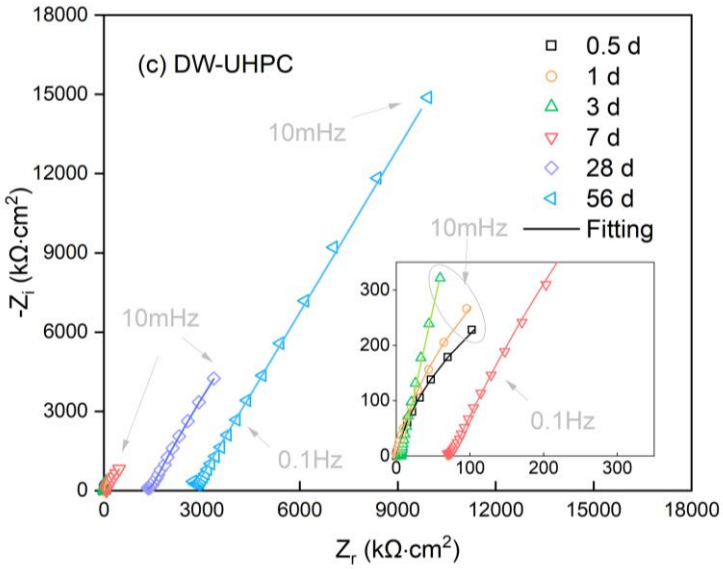
(c) DW-UHPC
0.5 d
1 d
3 d
7 d
28 d
56 d
Fitting
10mHz
10mHz
10mHz
0.1Hz
0.1Hz
-Z_i (kΩ·cm²)
Z_r (kΩ·cm²)

320

321

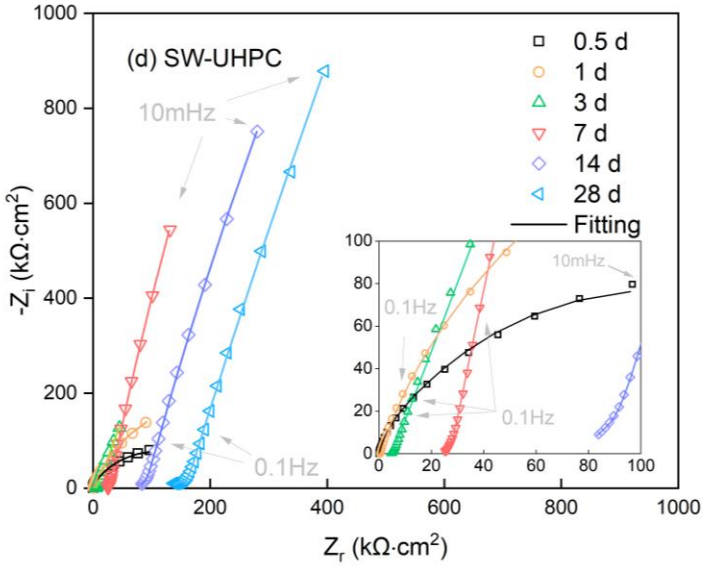
(d) SW-UHPC
0.5 d
1 d
3 d
7 d
14 d
28 d
Fitting
10mHz
10mHz
0.1Hz
0.1Hz
0.1Hz
-Z_i (kΩ·cm²)
Z_r (kΩ·cm²)

322

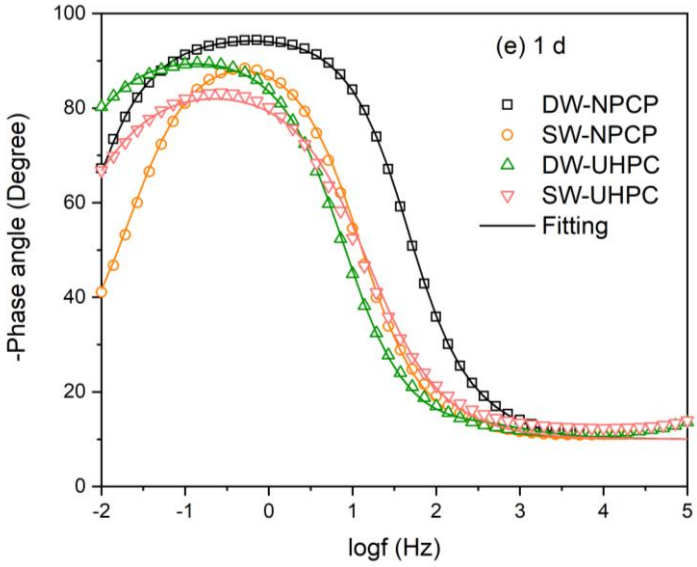

Fig. 5. EIS results of carbon steels in different cement pastes.

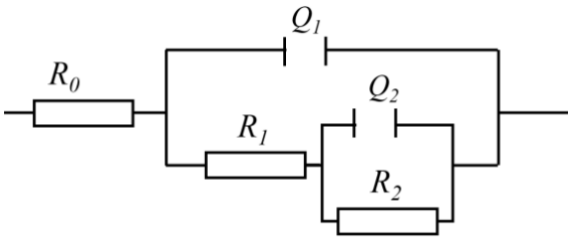

Fig. 6. Equivalent circuit for simulation of EIS results.

Table 5

Fitting results of EIS parameters for carbon steel in cement pastes.

ID	Time (d)	R_0 (Ω cm^2)	Y_0 (Q_{dl}) (S·sec^n·cm^{-2})	n_2	R_1 (kΩ cm^2)	Y_0 (Q_f) (S·sec^n·cm^{-2})	n_1	R_2 (kΩ cm^2)	R_p (kΩ cm^2)
DW-NPCP	0.5	103±3.2	(1.654±0.02)×10^{-5}	0.94±0.03	0.05±0.01	(0.520±0.001)×10^{-5}	0.945±0.01	842±11	841.95
	1	201±5.1	(1.325±0.01)×10^{-5}	1±0.00	0.33±0.01	(0.761±0.01)×10^{-5}	0.86±0.01	1182±23	1182.33
	3	400±8.2	(1.902±0.03)×10^{-5}	0.95±0.01	274.80±3.24	(1.008±0.01)×10^{-5}	0.73±0.01	1149±12	1423.80
	7	521±7.2	(1.887±0.02)×10^{-5}	0.95±0.03	253.60±2.12	(1.012±0.01)×10^{-5}	0.70±0.01	2599±24	2852.60
	28	696±13.0	(2.026±0.01)×10^{-5}	0.95±0.02	290.00±1.31	(0.982±0.01)×10^{-5}	0.68±0.01	3430±13	3471.00
	56	756±18.5	(2.338±0.05)×10^{-5}	0.95±0.01	251.30±5.12	(1.122±0.03)×10^{-5}	0.69±0.01	3569±54	3662.95

SW-NPCP	0.5	67 ± 0.8	(4.809±0.01) ×10^{-5}	0.91± 0.01	55.70± 0.33	(3.283±0.03) ×10^{-4}	0.98±0.01	18±1	73.60
	1	170± 2.1	(4.257 ±0.05) ×10^{-5}	0.93± 0.03	67.35± 1.12	(7.246±0.05) ×10^{-4}	0.99±0.01	12±1	79.74
	3	369± 3.1	(3.842±0.06) ×10^{-5}	0.94± 0.03	116.90± 3.53	(5.452±0.23) ×10^{-4}	0.98±0.01	28±1	144.86
	7	472 ± 2.3	(3.302±0.04) ×10^{-5}	0.96± 0.02	410.10± 2.98	(0.942±0.01) ×10^{-4}	0.95±0.01	203±2	613.10
	28	1084 ± 8.2	(2.657 ±0.08 ×10^{-5}	0.85± 0.02	142.70± 1.21	(0.126±0.01) ×10^{-4}	0.99±0.01	332±2	474.70
	56	760 ± 26.2	(4.302±0.07) ×10^{-5}	0.93± 0.05	157.90± 0.71	(2.702±0.01) ×10^{-4}	0.96±0.01	50±1	207.72
DW-UHPC	0.5	46 ± 0.7	(4.00±0.02)× 10^{-5}	0.87± 0.01	0.06± 0.001	(0.751±0.01) ×10^{-5}	0.98±0.01	533±12	533.46
	1	647 ± 5.3	(1.40 ±0.01) ×10^{-5}	0.87 ± 0.02	0.10± 0.002	(2.684±0.02) ×10^{-5}	0.94±0.01	1340±14	1340.10
	3	5656 ± 55.6	(1.64 ±0.02) ×10^{-5}	0.91 ± 0.03	1.48± 0.01	(2.172±0.01) ×10^{-5}	0.91±0.02	13650±62	13651.48
	7	69690 ±285.2	(0.61±0.01) ×10^{-5}	0.72 ± 0.03	33.81± 0.04	(3.104±0.01) ×10^{-6}	0.92±0.01	33410± 123	33443.81
	36	1363000 ±1976	(0.10±0.01) ×10^{-5}	0.81± 0.02	429.70± 1.3	(0.798±0.01) ×10^{-6}	0.72±0.01	82300± 112	82729.70
	56	2651000 ±1328	(0.01±0.01)× 10^{-5}	0.80± 0.04	467.00 ± 3.4	(0.359±0.01) ×10^{-6}	0.74±0.02	231700± 234	232167.00
SW-UHPC	0.5	51 ± 1.5	(4.909±0.04) ×10^{-5}	0.90± 0.01	61.96± 0.23	(4.90±0.03)× 10^{-5}	0.77±0.03	116±3	178.26
	1	349 ± 14.2	(0.982±0.01) ×10^{-5}	0.79± 0.01	0.07± 0.001	(4.93±0.05)× 10^{-5}	0.85±0.01	414±2	413.77
	3	4264 ± 47.2	(5.347±0.03) ×10^{-5}	0.85± 0.01	4.37± 0.01	(3.14±0.01)× 10^{-5}	0.78±0.01	8146±13	8150.37
	7	21680 ±38.2	(1.158±0.03) ×10^{-5}	0.93± 0.02	7.01± 0.02	(1.40±0.02) ×10^{-5}	0.88±0.01	14300±84	14307.01
	14	67700 ±292.2	(0.567±0.01) ×10^{-5}	0.91± 0.02	21.99± 0.10	(1.09±0.03)× 10^{-5}	0.85±0.02	17200±42	17221.99
	28	120000 ± 1298	(0.334±0.01) ×10^{-5}	0.87± 0.01	31.41± 0.03	(1.04±0.01)× 10^{-5}	0.87±0.01	20810±35	20841.41

The evolution of the resistivity of cement paste (R_0), which is a critical parameter for the corrosion rate of steel [64], is shown in **Fig. 7**. The initial resistivity of the cement paste was in the order of SW-UHPC < DW-UHPC < SW-NPCP < DW-NPCP. At the beginning, the paste was in the fresh state, and the resistivity of the paste was mainly controlled by the conductivity of the pore solution. The high salinity of

the pore solution in SW cement pastes would lead to lower resistivities. The rapid consumption of the limited amount of water by cement hydration in UHPC further induced a very high salinity of the pore solution. The initial pH values of UHPCs were much higher than the NPCPs as shown in **Fig. 1(a)**. This was the reason for the lower resistivities of the fresh UHPCs compared with NPCPs. Nevertheless, the resistance of the paste in UHPCs increased sharply, and it became higher than those of NPCPs after 12 h. It was due to the dense matrix, consumption of the limited amount of water in the pores and the significant reduction of the internal humidity caused by self-desiccation [13].

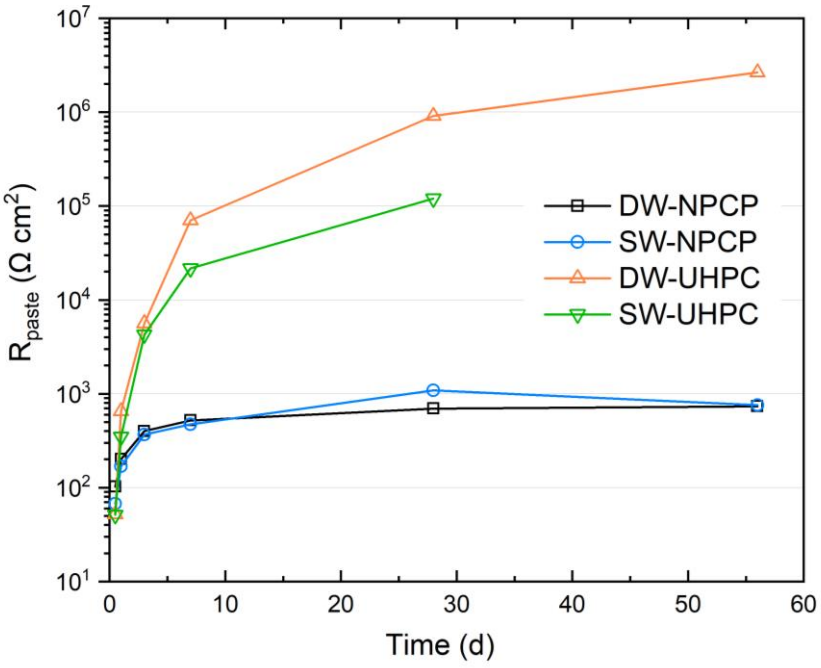

Fig. 7. Resistivity of cement pastes as a function of time.

At 28 d, the resistivity of the paste in DW-UHPC reached 1×10^6 Ωcm^2, which was three orders of magnitude higher than those of the NPCPs and one order of magnitude higher than that of SW-UHPC. This can also be observed from the Z_f value corresponding to the minimum Z_i value in the high frequency region of the Nyquist plots. It should be noted that the resistance of the SW-UHPC was too high to obtain readable EIS curves after 28 d. In this case, the internal relative humidity of SW-UHPC should be too low for the corrosion of carbon steel. For the SW-NPCP specimen, the resistivity was slightly lower than that

of DW-NPCP within 14 d. It might be attributed to the high salinity (very low resistivity as confirmed in literature [50]) of the pore solution in SW-NPCP as shown in **Figs. 1 and 2**, even though the cross-sectional fraction of the electrolyte channels was reduced by the refined pore structure of the paste prepared with seawater as shown in **Fig. 4**. After 14 d, the resistivity of SW-NPCP became higher than the DW-NPCP but reduced again to reach a similar level to DW-NPCP. This fluctuation might be due to the change of the pore structure caused by the crystallization of salts in the seawater cement paste [65].

The R_1 and R_2 values of specimens in DW cement pastes increased with time, which is in agreement with the trend of passivation process of steel bar reported in previous work [33, 66]. Higher values of R_1 were obtained in DW-UHPC, and the R_2 values were almost two orders of magnitude higher after 56 d. It was mainly because the lack of water resulted in the reduction of effective exposed area of steel. For SW-NPCP, the R_1 and R_2 values decreased after 28 d and 56 d respectively. This phenomenon could be attributed to the reduction of resistivity of cement paste as described above. For SW-UHPC, the R_1 values were much lower than those in SW-NPCP. The R_1 values were related to the mass and chemistry of the corrosion products, which was discussed in the following sections. R_2 value in SW-UHPC after 56 d was three orders of magnitude higher than those of SW-NPCP. R_2 was closely related to the anodic or cathodic process of corrosion. The redox process of the corrosion products on steel surface would support the cathodic process even though the oxygen was limited. The presence of the Cl^- would promote the anodic process of corrosion in SW-UHPC, however the extremely limited water supply would inhibit the anodic process of corrosion, resulting in much higher R_2 values.

3.2.2 Open circuit potential and corrosion rate

To obtain the corrosion behavior of the carbon steel, the corrosion rate i_{corr}, which is related to the polarization resistance, was obtained according to ASTM G59 [67]:

$$i_{corr} = B/R_p \qquad (3)$$

where B is the Stern-Geary constant. The B value used to calculate the corrosion rate was 26 mV for the active corrosion condition in SW-NPCP and SW-UHPC and 52 mV for the passive state in DW-NPCP and DW-UHPC in the present work [68, 69]. The polarization resistance R_p was calculated using the following equation [70]:

$$R_p = R_1 + R_2 \qquad (4)$$

It should be noted that the R_p values increased to an extremely high level in SW-UHPC after 3 d as shown in **Table 5**, which can be regarded as similar to the level of a passive state. The B value of 52 mV was thus selected to calculate the corrosion rate after 3 d.

The evolutions of open circuit potential and the corrosion rate of carbon steel in different cement pastes are shown in **Fig. 8**. For DW-NPCP, the initial potential of the carbon steel was negative of ca. -0.3 V, which indicates the oxidation reaction between the bare carbon steel and the highly alkaline pore solution in the cement paste. The potential increased immediately, indicating the formation of an oxide film (passive film) on the steel in the cement paste. After ca. 7 d, the potential almost stabilized which suggested that a full oxide film was formed on the steel surface. The slight increase of the potential with time was due to the compacting and thickening of the passive film. It can also be confirmed by the evolution of the corrosion rate of the DW-NPCP. The corrosion rate of the carbon steel reduced with time at the beginning. After ca. 14 d, it became steady at a very low level, indicating a fully passive state of the carbon steel in cement paste. This trend represented the general passivation process of the carbon steel in the concrete without any contamination and was consistent with the passivation process in normal-performance cement mortar and the simulated concrete pore solutions [71-73].

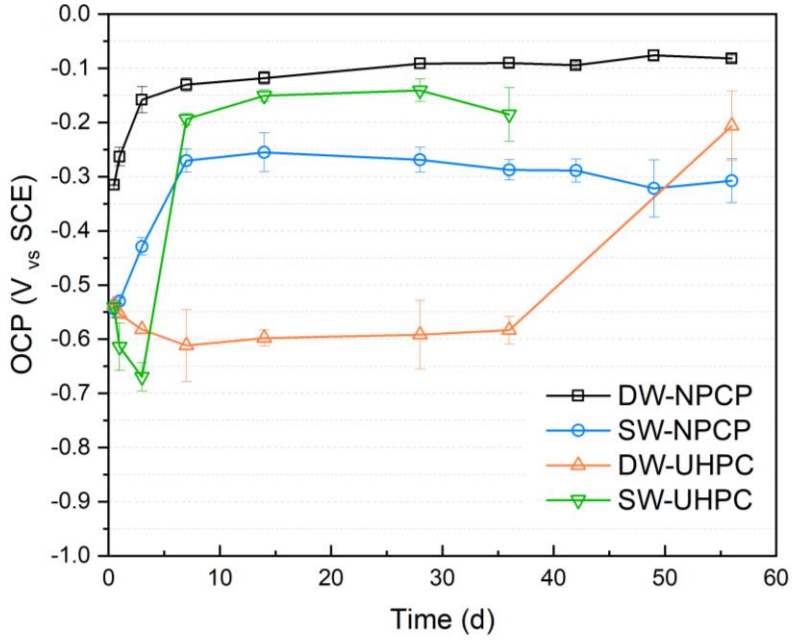

(a)

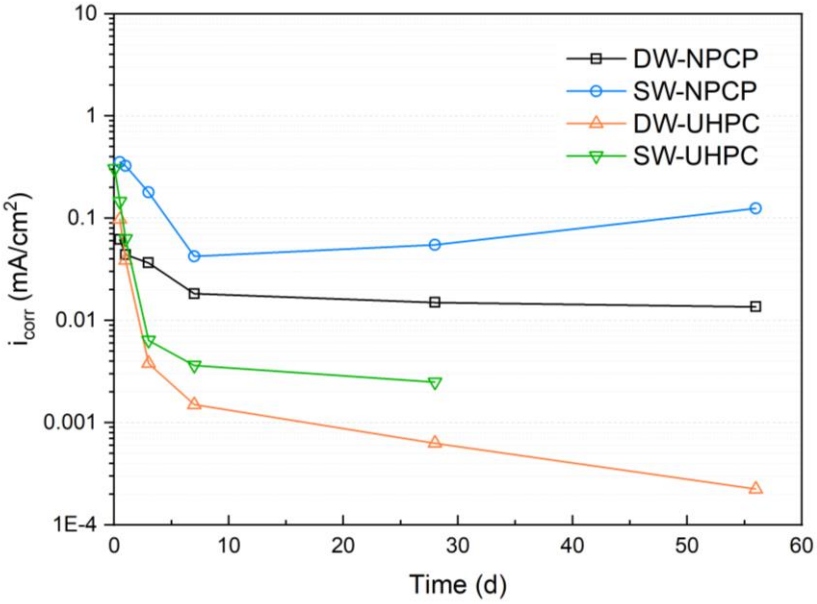

(b)

Fig. 8. Evolution of (a) open circuit potential and (b) corrosion rate of carbon steel as a function of time.

For SW-NPCP, the initial potentials were much more negative than that in DW-NPCP, and the corrosion rates were at a very high level, indicating that the carbon steel was in an active corrosion state at the

beginning. This was due to the high Cl^-/OH^- ratio in the pore solution of the cement paste as shown in **Fig. 2**. The concentration of the OH^- in the pore solution was not sufficient to promote the passivation of the carbon steel. Subsequently, the potential in SW-NPCP increased significantly to a high level within 14 d, suggesting a reduction of the corrosion probability of the carbon steel. Simultaneously, the corrosion rate decreased significantly to a very low level. This was mainly due to the decrease of the Cl^-/OH^- ratio with time as shown in **Fig. 2**, reducing the corrosivity of the pore solution. The increase of the resistivity of the cement paste might also contribute to the decrease of the corrosion rate and the positive shift of the potential. After 28 d, the potential decreased slightly, and the corrosion rate increased gradually. This was due to the reduction of the resistivity of cement paste, which was caused by the change of the microstructure as described above.

For DW-UHPC, the initial potential of around -0.550 V was much more negative compared with DW-NPCP. This was further shifted to the negative direction in 7 days and tended to be stabilized at -0.600 V subsequently. At the beginning, the fresh cement paste had sufficient water and dissolved oxygen and a higher pH value resulted in more negative potential due to the partial dissolution of passive film with the increase of the alkalinity of solution following the relation [74]:

$$E = a - b\,\mathrm{pH} \qquad (5)$$

where a and b (have a value ~30 mV/pH unit) are constants. The dissolution of passive film occurred according to:

$$Fe(OH)_2 + OH^- = FeO_2^- + H_2O \qquad (6).$$

Therefore, the negative initial potential was attributed to the high initial pH value of the pore solution in DW-UHPC as shown in **Fig. 1(a)**.

With the hydration of cement, the microstructure of DW-UHPC became much denser within a short period, and the supply of the oxygen would be restricted. The subsequent negative shift was expected to be due to the gradually limited oxygen supply according to the Evans diagram as shown in **Fig. 9(a)** [19].

The potential is dominated by the cathodic reaction process, which is determined by the oxygen diffusion at the steel/paste interface.

In **Fig. 8(b)**, the corrosion rate decreased starting from the very beginning to extremely low level at 3 d. This level was one order of magnitude lower than that of DW-NPCP. Generally, a negative potential is believed to be associated to an active corrosion state. But the oxygen availability should be considered also when analyzing the corrosion behavior of steel in such a dense cementitious matrix [19]. It is interesting that the potential suddenly shifted to a much positive value after 36 d, while the trend of the corrosion rate did not change. According to the corrosion rate, it could be known that the steel remained in a passive state after 36 d. The oxygen supply was supposed to remain in a limited state with cement hydration. If the potential was dominated by the cathodic reaction, the potential would be negative. With the progress of the cement hydration the passivation process would proceed on even with limited oxygen supply, which could be reflected in the R_1 values in **Table 5**. Therefore, it could be proposed that the potential of the steel was dominated by the anodic reaction process, since the formation of a dense passive film inhibited the anodic reaction. The mechanism can be illustrated by the Evans diagram as shown in **Fig. 9(b)**.

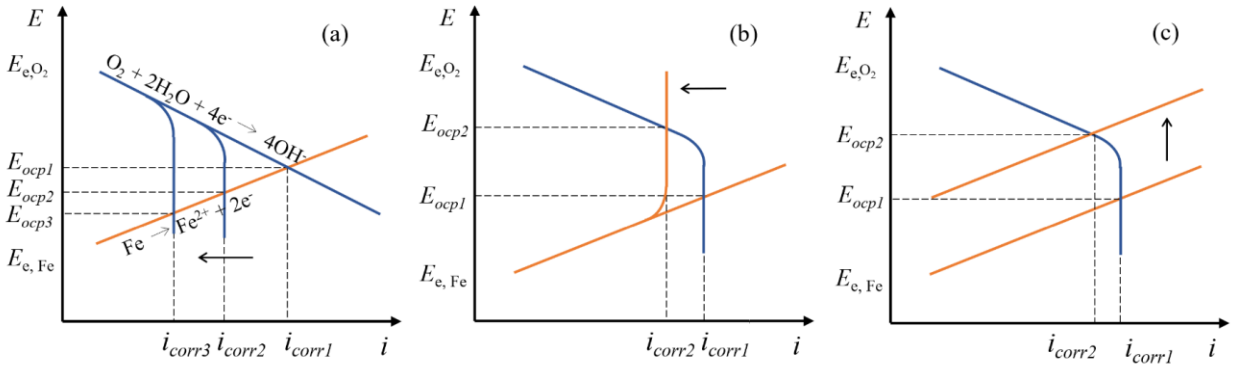

Fig. 9. Evans diagram of mixed potential E vs. current density i. (a) decrease of O_2 supply, (b) enhancement of passive film, (c) increase of Fe^{2+} concentration.

For SW-UHPC, the potential started off at a negative level at around -0.670 V, and then increased sharply to a very positive level. However, the corrosion rate decreased significantly to a very low level, which was not consistent with the evolution of the potential. The OCP is a mixed potential when the anodic and cathodic reaction rates are equal (with zero current), and it in part or in whole reflects the chemistry of the internal cement paste environment surrounding the carbon steel [75]. The high initial Cl^-/OH^- ratio in SW-UHPC (**Fig. 2(b)**) and the high initial corrosion rate in **Fig. 8(b)** indicated an actively corrosion state of the carbon steel at the beginning, which corresponded to the initial low OCP value. The shift to the negative direction within 3 d was attributed to the gradually reduction of oxygen supply with the hydration of cement as illustrated in **Fig. 9(a)**. A sharp shift of potential to positive values close to those of passivated steel in DW-NPCP occurred after 3 d, implying that the OCP changed to be controlled by the anodic reaction. With the cement hydration, the microstructure of cement paste became ultra-dense, and the water would be consumed gradually. The transport of the ions formed at the site of corrosion to the cement paste matrix would be inhibited, resulting in the sharp increase of the concentration of the ions at the steel surface. It is known that the corrosion of steel and related Nernst equation could be expressed as [76, 77]:

Anodic reaction

$$Fe \rightarrow Fe^{2+} + 2e^- \quad (7)$$

$$E_{Fe/Fe^{2+}} = E_0 + \frac{RT}{2F} lnFe^{2+} \quad (8)$$

Cathodic reaction

$$O_2 + 2H_2O + 4e^- \rightarrow 4OH^- \quad (9)$$

$$E_{O_2/OH^-} = E_0 + \frac{RT}{4F} ln \frac{O_2}{OH^-} \quad (10)$$

The concentrated Fe^{2+} at the steel surface **(equations (7) and (8))** will increase the reversible potential and inhibit the anodic reaction. This is the cause for the increase of the OCP values to positive level

around -0.150 V after 7 d based on the Evans diagram as shown in **Fig. 9(c)**. It is worth noting that the insufficient oxygen supply was not a main factor inhibiting the corrosion process, since the conversion of the corrosion products in different phases could also sustain the cathodic reaction of the corrosion process. Therefore, the lack of water was suspected to account for the mitigation of the corrosion in SW-UHPC.

3.2.3 Surface characterization of carbon steel

Fig. 10 displays the representative surface morphologies of the carbon steels in SW-NPCP and SW-UHPC after 56 d of curing. For the SW-NPCP in **Fig. 10(a)**, a large amount of hydration products, including C-S-H (gel phase) and $Ca(OH)_2$ (plate-like phase, CH), could be observed on the carbon steel surface. It thus confirmed the presence of a lime-rich layer at the steel/paste interface, which was known to exhibit a buffering effect for maintaining the pH value of the pore solution in concrete and was beneficial for the inhibition of the corrosion initiation induced by the chloride ions. However, as shown in **Fig. 10(a)** for SW-NPCP, the CH crystals in this lime-rich layer were only loosely attached on the steel surface, but the corrosion products were firmly formed on the steel surface. This was because the growth of the products was limited by the hardened paste surrounding the steel. In contrast, for the SW-UHPC in **Fig. 10(b)**, the loosely distributed corrosion products protruded outwards, indicating that the corrosion occurred before the set of the cement paste, which was in agreement with the electrochemical test results in **Fig. 8**.

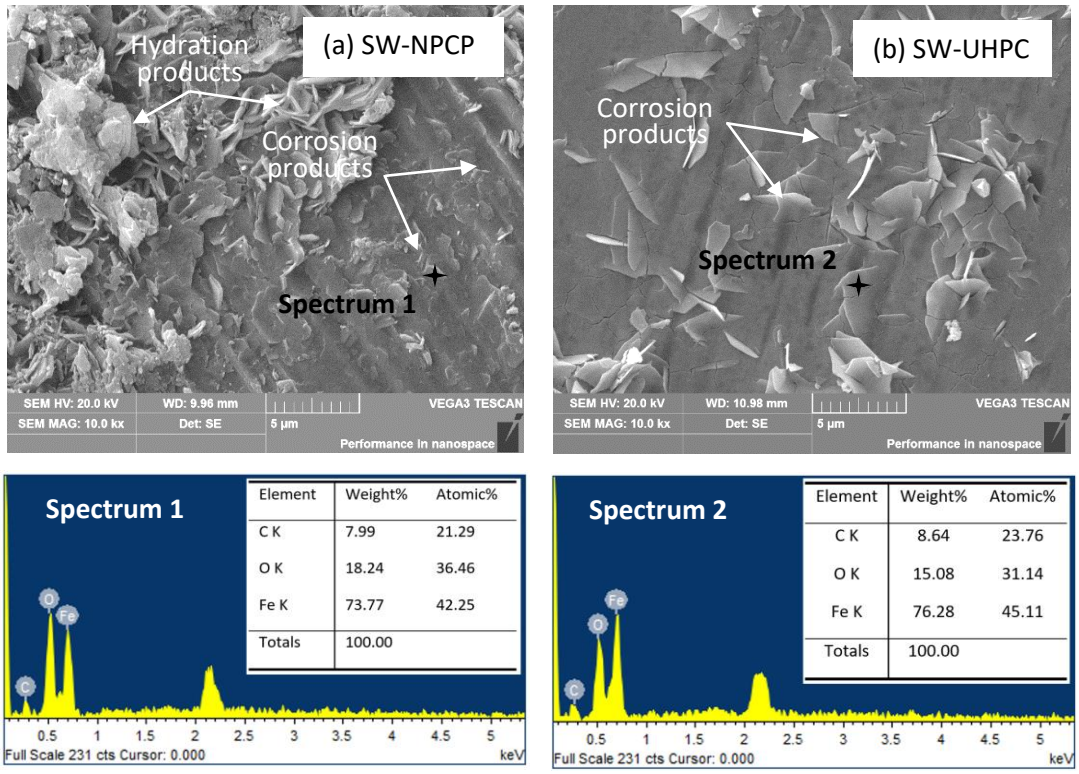

Fig. 10. Surface morphologies of carbon steels in SW-NPCP and SW-UHPC.

To characterize the surface condition of carbon steel in DW-NPCP and DW-UHPC, XPS is a powerful method to characterize the chemistry of the passive film formed. **Figs. 11** and **12** are the survey spectra and high resolution XPS spectra of Fe $2p_{3/2}$ on the carbon steel in the studied cement pastes. **Table 6** shows the detailed proportion of the decomposition and thicknesses of the passive films. The high-resolution spectra was fitted , and the thickness of passive film was calculated according to the equation reported in the literature [33, 78]. A thicker passive film with a higher Fe^{3+}/Fe^{2+} ratio and Fe_{oxides} proportion (**Table 6**) was obtained on the carbon steel in DW-UHPC compared with DW-NPCP. At the later age, the availability of oxygen was limited in DW-UHPC and it would not be favorable for the growth of passive film. Therefore, the initial high pH value accounts for the rapid formation of a thicker passive film with higher proportion of Fe^{3+} oxides. The structure of Fe^{3+} oxides was more porous, and the Fe^{2+} oxides in the passive film were proved to be more protective [79]. The passive film formed in DW-NPCP would be more protective despite that it was thinner. The much higher R_p value in DW-UHPC

NPCP was expected to be due to the much less cross-sectional fraction of the electrolyte channel for which resulted in a lower effective exposed area as mentioned above.

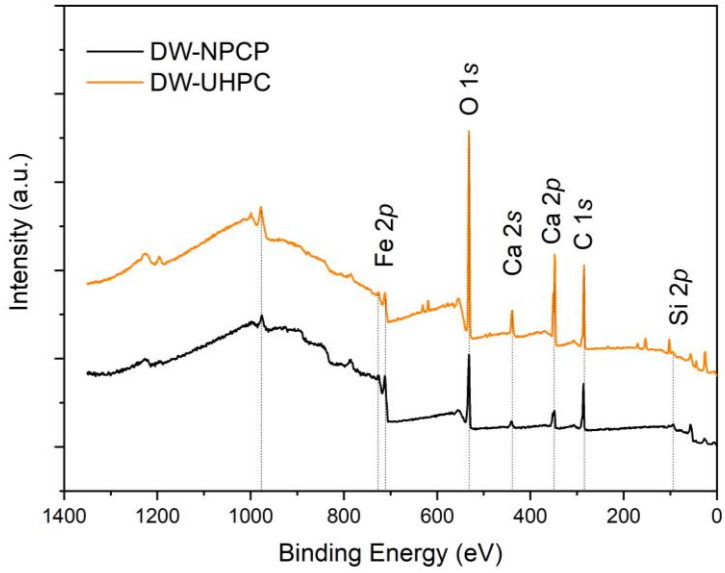

Fig. 11. Survey spectra of carbon steel in DW-NPCP and DW-UHPC after 56 d of curing.

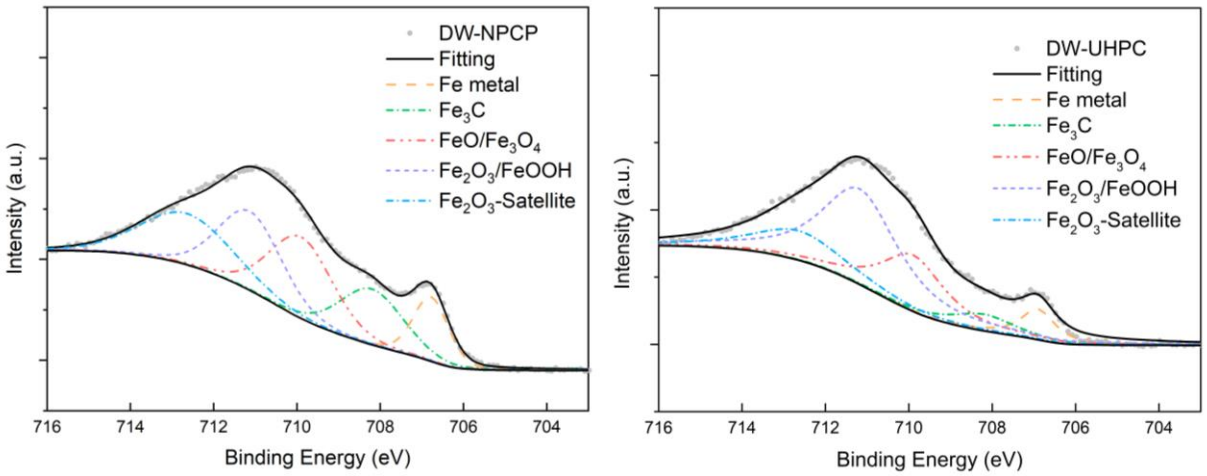

(a) (b)

Fig. 12. High resolution XPS spectra of Fe 2p3/2 on steel in (a) DW-NPCP and (b) DW-UHPC.

Table 6

Proportions of decomposition and thicknesses of passive films.

Samples	Fe^{3+}/Fe^{2+}	Fe_{metal} (%)	Fe^{2+}/Fe_{oxides}	Fe_{oxides} (%)	Thickness (nm)

DW-NPCP	1.881	10.9	0.347	71.9	6.13
DW-UHPC	2.833	6.8	0.261	86.5	8.02

507

508 3.2.4 Steel/paste interface model

509 The characteristic of the steel/concrete interface also plays an important role in the corrosion initiation of
510 steel [4, 8, 80]. According to the results of the present work, a model of steel/seawater cement paste
511 interface is proposed as shown in **Fig. 13**. For fresh cement pastes prepared by using seawater, the steel is
512 directly surrounded by the pore solution of the pastes which is similar to that in the simulated pore
513 solution contaminated with aggressive ions of the seawater. However, after hardening, the steel/paste
514 interface is quite different for different pastes. For the SW-NPCP specimens, the paste matrix would be
515 much denser than that of the DW-NPCP specimens. For the UHPCs, the dense and compacted
516 cementitious pastes would result in a low porosity (**Fig. 4**), and the self-desiccation of the UHPC would
517 also produce a very low internal relative humidity [13]. Due to the extremely low permeability and
518 unsaturated condition of the pores in UHPC, the transport of the aggressive ions, water and oxygen would
519 be significantly restrained. While the availabilities of water and oxygen would be dominant factors
520 influencing the corrosion process of steel in UHPC specimens. Furthermore, it is suspected that the lime-
521 rich layer at the interface would not be present in UHPC specimens due to the low CH content. This was
522 evidenced by the ultra-low CH content (2.61%) as shown in **Table 2**.

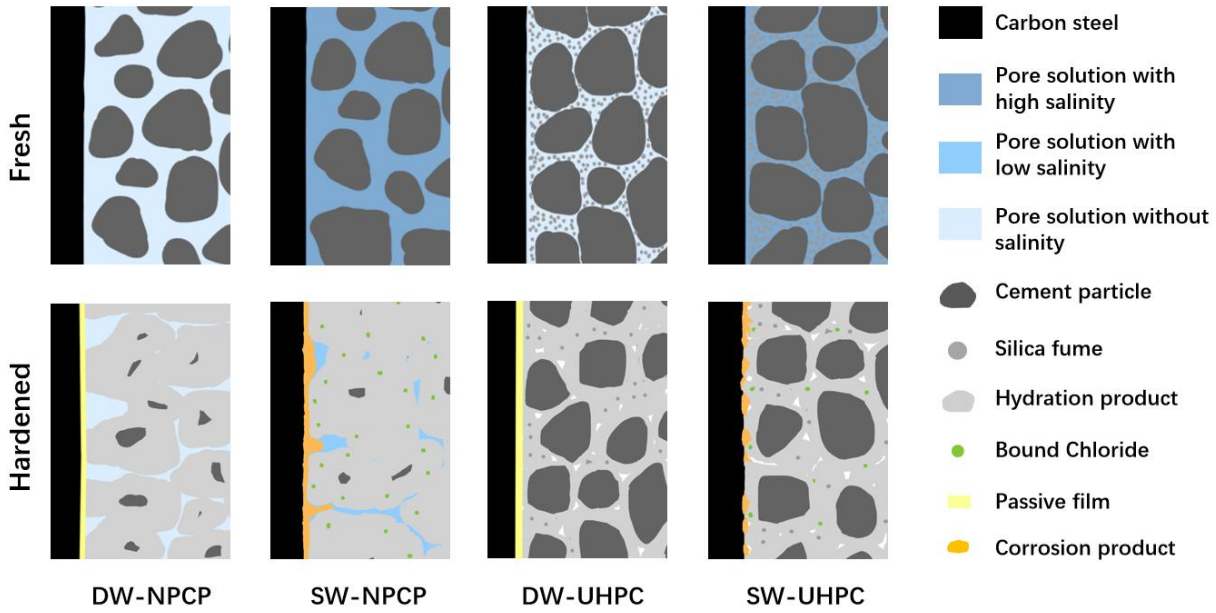

Fig. 13. Model of steel/paste interface in fresh and hardened cement pastes.

3.3 General discussion

The corrosion behavior of carbon steel is closely related to the internal environment of concrete. For the concrete prepared with seawater, the corrosion of the bare steel was initiated immediately after the casting of the concrete, which was mainly attributed to the high initial Cl^-/OH^- ratio in the pore solution. With the development of the cement hydration, the chloride content (aggressive factor) in the pore solution increased sharply at the beginning and then decreased significantly to a much lower level, and the majority of the chloride ion was bound by the hydration products. Simultaneously, the pH value and the resistivity of the paste (inhibiting factor) increased with time. These resulted in an exponential decrease of the Cl^-/OH^- ratio, implying a reduction of the corrosion risk for the carbon steel. In spite of this, the buffering effect of the lime-rich layer on the reduction of the pH value, which may have positive effect on the corrosion inhibition, should also be considered. However, corrosion could not be ceased in the SW-NPCP after the hardening of the cement paste. The OH^- concentration in the pore solution is not high enough to inhibit the corrosion process, and the relatively lower resistivity of paste was also a contributing factor for the corrosion propagation of carbon steel. In DW-UHPC, passivation occurred and

a strong passive film was formed, even though the oxygen supply was limited after the hardening of the cement paste.

The corrosion rate of the carbon steel in SW-UHPC was high but fell to a negligible level within the first several days. It could be mainly due to the very high resistivity caused by the low internal humidity and dense microstructure. It is not the insufficient oxygen supply but the lack of water that inhibited the corrosion process of the carbon steel. To some extent, UHPC, even with admixed Cl^-, may act as an insulating (ultra-high resistivity) material protecting the steel from corrosion. In this work, the influence of the admixed chloride in SW-UHPC was investigated. The corrosion behavior of steel bar in SW-UHPC with the attack of the external chloride remains unknown. The chloride threshold value in such cementitious materials is also an interesting point to be studied. Furthermore, it should also be emphasized that the corrosion risk would be high when crack is induced in UHPC contaminated with Cl^-. Both the leaching of Cl^- and OH^- from cement paste matrix will be present after the ingress of water, and the steel bar is in active state according to the finding in this work. The initial corrosion risk of steel bar exposed to cracks will be very high due to the presence of chloride ion and sufficient supply of water and oxygen. However, the inhibiting agent OH^- will be high due to the secondary hydration of unhydrated cement particles in UHPC matrix. The initial corrosion behavior of steel in cracks largely depends on the Cl^-/OH^- ratio of the micro-environment in the crack. Further studies on the corrosion behavior of steel bar in UHPC with cracks is urgently needed in the future.

4. Conclusions

The present work investigated the corrosion behavior of carbon steel in severely chloride-contaminated ultra-high-performance cement pastes. The following conclusions can be drawn:

1) The initial Cl^-/OH^- ratios in the pore solutions of SW-NPCP and SW-UHPC were higher than the critical values of 0.6, thus the corrosion of carbon steel occurred. The Cl^- concentration increased sharply to 0.7 mol/L at the beginning and then decreased exponentially to a low level with the hydration of the

cement in SW-NPCP. More than 86% and 92% of the chloride ions was chemically and physically bounded by the cement hydration products in SW-NPCP and SW-UHPC respectively.

2) Even though oxygen supply was limited due to the ultra-dense microstructure after the hardening of the cement paste, a well passivated state of the carbon steel was achieved in DW-UHPC due to the initial high alkalinity of the pore solution, of which the pH value was higher than 13.4. A thicker passive film (8.02 nm) with higher corrosion resistance was attained on the carbon steel in DW-UHPC compared with DW-NPCP.

3) Corrosion of the carbon steel in seawater mixed cement pastes (SW-NPCP and SW-UHPC) occurred after the casting of cement pastes. The corrosion process in SW-NPCP continued due to the presence of chloride ion and lower resistivity of the paste. However, the corrosion in SW-UHPC was significantly inhibited within the first 3 days mainly due to the lack of water for the electrochemical process.

Data Availability Statement

Some or all data, models, or code that support the findings of this study are available from the corresponding author upon reasonable request.

Acknowledgements

The work described in this paper was partially supported by a grant from the Research Grants Council of the Hong Kong Special Administrative Region (Project No. T22-502/18-R). The authors gratefully acknowledge the financial support of Hong Kong Branch of the National Engineering Research Center for Steel Construction. The last author also acknowledge the support of National Natural Science Foundation of China (51879292) and the Guangdong International Science and Technology Cooperation Program (2019A050510020).

References

[1] M. Stefanoni, U.M. Angst, B. Elsener, Kinetics of electrochemical dissolution of metals in porous media, Nature materials, (2019).

[2] M. Stefanoni, U.M. Angst, B. Elsener, Electrochemistry and capillary condensation theory reveal the mechanism of corrosion in dense porous media, Scientific reports, 8 (2018) 7407.

[3] G. Samson, F. Deby, J.-L. Garciaz, M. Lassoued, An alternative method to measure corrosion rate of reinforced concrete structures, Cem. Concr. Compos., (2020).

[4] U.M. Angst, M.R. Geiker, M.C. Alonso, R. Polder, O.B. Isgor, B. Elsener, H. Wong, A. Michel, K. Hornbostel, C. Gehlen, R. François, M. Sanchez, M. Criado, H. Sørensen, C. Hansson, R. Pillai, S. Mundra, J. Gulikers, M. Raupach, J. Pacheco, A. Sagüés, The effect of the steel–concrete interface on chloride-induced corrosion initiation in concrete: a critical review by RILEM TC 262-SCI, Mater. Struct., 52 (2019).

[5] A. Kenny, A. Katz, Influence of the Interfacial Transition Zone Properties on Chloride Corrosion in Reinforced Concrete-Characterization of ITZ, Advanced Materials Research, 95 (2010) 69-72.

[6] C.L. Page, Initiation of chloride-induced corrosion of steel in concrete: role of the interfacial zone, Mater. Corros., 60 (2009) 586-592.

[7] T.A. Soylev, R. François, Quality of steel–concrete interface and corrosion of reinforcing steel, Cem. Concr. Res., 33 (2003) 1407-1415.

[8] U.M. Angst, M.R. Geiker, A. Michel, C. Gehlen, H. Wong, O.B. Isgor, B. Elsener, C.M. Hansson, R. François, K. Hornbostel, R. Polder, M.C. Alonso, M. Sanchez, M.J. Correia, M. Criado, A. Sagüés, N. Buenfeld, The steel–concrete interface, Mater. Struct., 50 (2017) 143.

[9] J. Ming, M. Wu, J. Shi, Passive film modification by concrete carbonation: Re-visiting a corrosion-resistant steel with Cr and Mo, Cem. Concr. Compos., 123 (2021).

[10] A.S. Al-Ameeri, M.I. Rafiq, O. Tsioulou, Combined impact of carbonation and crack width on the Chloride Penetration and Corrosion Resistance of Concrete Structures, Cem. Concr. Compos., 115 (2021).

[11] R.E. Melchers, I.A. Chaves, Reinforcement Corrosion in Marine Concretes—1: Initiation, ACI Mater. J., 116 (2019).

[12] N.M. Azmee, N. Shafiq, Ultra-high performance concrete: From fundamental to applications, Case Stud. Constr. Mater., 9 (2018) e00197.

[13] P. Shen, L. Lu, F. Wang, Y. He, S. Hu, J. Lu, H. Zheng, Water desorption characteristics of saturated lightweight fine aggregate in ultra-high performance concrete, Cem. Concr. Compos., 106 (2020) 103456.

[14] P. Shen, H. Zheng, D. Xuan, J.-X. Lu, C.S. Poon, Feasible use of municipal solid waste incineration bottom ash in ultra-high performance concrete, Cem. Concr. Compos., 114 (2020).

[15] J.-X. Lu, P. Shen, H. Zheng, H.A. Ali, C.S. Poon, Development and characteristics of ultra high-performance lightweight cementitious composites (UHP-LCCs), Cem. Concr. Res., 145 (2021).

[16] P. Shen, J.-X. Lu, H. Zheng, L. Lu, F. Wang, Y. He, S. Hu, Expansive ultra-high performance concrete for concrete-filled steel tube applications, Cem. Concr. Compos., 114 (2020).

[17] J. Li, Z. Wu, C. Shi, Q. Yuan, Z. Zhang, Durability of ultra-high performance concrete – A review, Constr. Build. Mater., 255 (2020).

[18] W. Wang, J. Liu, F. Agostini, C.A. Davy, F. Skoczylas, D. Corvez, Durability of an Ultra High Performance Fiber Reinforced Concrete (UHPFRC) under progressive aging, Cem. Concr. Res., 55 (2014) 1-13.

[19] L. Fan, W. Meng, L. Teng, K.H. Khayat, Effect of steel fibers with galvanized coatings on corrosion of steel bars embedded in UHPC, Composites Part B: Engineering, 177 (2019).

[20] E. Ghafari, M. Arezoumandi, H. Costa, E. Júlio, Influence of nano-silica addition on durability of UHPC, Constr. Build. Mater., 94 (2015) 181-188.

[21] N. El-Joukhadar, S.J. Pantazopoulou, Effectiveness of UHPFRC cover in delaying bar corrosion, Constr. Build. Mater., (2020).

[22] G.Y. Koga, P. Comperat, B. Albert, V. Roche, R.P. Nogueira, Effect of endogenous chloride contamination on the electrochemical and hydration responses of reinforced Belite-Ye'elimite-Ferrite (BYF) cement mortars, Cem. Concr. Res., 122 (2019) 212-226.

637 [23] A. Kayyali, M.N. Haque, The Cl^-/OH^- ratio in chloride-contaminated concrete — a most important
638 criterion, Magazine of Concrete Research, 47 (1995) 235-242.
639 [24] D.A. Hausmann, A probability model of steel corrosion in concrete, Materials Performance, 37
640 (1998) 64-68.
641 [25] P. Lambert, C. L. Page, P.R.W. Vassie, Investigations of reinforcement corrosion. 2. Electrochemical
642 monitoring of steel in chloride-contaminated concrete, Mater. Struct., 24 (1991) 351-358.
643 [26] W. Feng, Z. Dong, W. Liu, H. Cui, W. Tang, F. Xing, An experimental study on the influence of
644 applied voltage on current efficiency of rebars with a modified accelerated corrosion test, Cem. Concr.
645 Compos., 122 (2021).
646 [27] A.K. Suryavanshi, J.D. Scantlebury, S.B. Lyon, Corrosion of reinforcement steel embedded in high
647 water-cement ratio concrete contaminated with chloride, Cement and Concrete Composites, 20 (1998)
648 263-381.
649 [28] R. Yu, P. Spiesz, H.J.H. Brouwers, Development of an eco-friendly Ultra-High Performance
650 Concrete (UHPC) with efficient cement and mineral admixtures uses, Cem. Concr. Compos., 55 (2015)
651 383-394.
652 [29] Z. Wu, K.H. Khayat, C. Shi, Changes in rheology and mechanical properties of ultra-high
653 performance concrete with silica fume content, Cem. Concr. Res., 123 (2019).
654 [30] T.U. Mohammed, H. Hamada, T. Yamaji, Performance of seawater-mixed concrete in the tidal
655 environment, Cem. Concr. Res., 34 (2004) 593-601.
656 [31] E. Redaelli, A. Arrigoni, M. Carsana, G. Dotelli, M. Gastaldi, F. Lollini, F. Bertola, F. Canonico, A.
657 Nanni, Culvert Prototype Made with Seawater Concrete: Materials Characterization, Monitoring, and
658 Environmental Impact, Advances in Civil Engineering Materials, 8 (2019).
659 [32] ASTM D1141-98, Standard Practice for the Preparation of Substitute Ocean Water, ASTM
660 International.
661 [33] H. Zheng, C.S. Poon, W. Li, Mechanistic study on initial passivation and surface chemistry of steel
662 bars in nano-silica cement pastes, Cem. Concr. Compos., 112 (2020).

663 [34] H. Zheng, J.-G. Dai, L. Hou, G. Meng, C.S. Poon, W. Li, Enhanced passivation of galvanized steel
664 bars in nano-silica modified cement mortars, Cem. Concr. Compos., 111 (2020).
665 [35] M. Kosalla, M. Raupach, Potential differences between passive reinforcement segments in concrete
666 components in dependency of binder type, aeration conditions and quality of the steel/concrete-interface,
667 Mater. Corros., 67 (2016) 639-651.
668 [36] M.A.B. J. Duchesne, Evaluation of the validity of the pore solution expression method from
669 hardened cement pastes and mortars, Cem. Concr. Res., 24 (1994) 456-462.
670 [37] G. Plusquellec, M.R. Geiker, J. Lindgård, J. Duchesne, B. Fournier, K. De Weerdt, Determination of
671 the pH and the free alkali metal content in the pore solution of concrete: Review and experimental
672 comparison, Cem. Concr. Res., 96 (2017) 13-26.
673 [38] A. Behnood, K. Van Tittelboom, N. De Belie, Methods for measuring pH in concrete: A review,
674 Constr. Build. Mater., 105 (2016) 176-188.
675 [39] A. Scott, M.G. Alexander, Effect of supplementary cementitious materials (binder type) on the pore
676 solution chemistry and the corrosion of steel in alkaline environments, Cem. Concr. Res., 89 (2016) 45-55.
677 [40] M.S. Ekkehard Fehling, Joost Walraven, Torsten Leutbecher, Susanne Frohlich, Ultra-high
678 performance concrete UHPC _ fundamentals, design, examples, BetonKalender series, Wiley, (2013).
679 [41] P. Shen, L. Lu, Y. He, F. Wang, J. Lu, H. Zheng, S. Hu, Investigation on expansion effect of the
680 expansive agents in ultra-high performance concrete, Cem. Concr. Compos., 105 (2020).
681 [42] S.-H. Kang, S.-G. Hong, J. Moon, Importance of drying to control internal curing effects on field
682 casting ultra-high performance concrete, Cem. Concr. Res., 108 (2018) 20-30.
683 [43] Chaussadent, G. Arliguie, AFREM test procedures concerning chlorides in concrete: Extraction and
684 titration methods, Mater. Struct., 32 (1999) 230-234.
685 [44] S. Rengaraju, L. Neelakantan, R.G. Pillai, Investigation on the polarization resistance of steel
686 embedded in highly resistive cementitious systems – An attempt and challenges, Electrochim. Acta,
687 (2019).

688 [45] R.R. Hussain, A. Al-Negheimish, A. Alhozaimy, D.D.N. Singh, Corrosion characteristics of
689 vanadium micro-alloyed steel reinforcement bars exposed in concrete environments and industrially
690 polluted atmosphere, Cem. Concr. Compos., 113 (2020).
691 [46] S. Diamond, Effects of Microsilica (Silica Fume) on Pore-Solution Chemistry of Cement Pastes,
692 Communications of the American Ceramic Society, 66 (1983) C-82-C-84.
693 [47] J.A. Larbi, A.L.A. Fraay, J.M.J.M. Bijen, The chemistry of the pore fluid of silica fume-blended
694 cement systems, Cem. Concr. Res., 20 (1990) 506-516.
695 [48] C.M.D. Lobo C, Hydration of type K expansive cement paste and the effect of silica fume: II. Pore
696 solution analysis and proposed hydration mechanism, Cem. Concr. Res., 23 (1993) 104-114.
697 [49] V.Ø. Page C L, Pore solution composition and chloride binding capacity of silica-fume cement
698 pastes, Matériaux et construction, 16 (1983) 19-25.
699 [50] L. Montanari, P. Suraneni, M. Tsui-Chang, M. Khatibmasjedi, U. Ebead, J. Weiss, A. Nanni,
700 Hydration, Pore Solution, and Porosity of Cementitious Pastes Made with Seawater, J. Mater. Civ. Eng.,
701 31 (2019).
702 [51] Y. Cai, D. Xuan, P. Hou, J. Shi, C.S. Poon, Effect of seawater as mixing water on the hydration
703 behaviour of tricalcium aluminate, Cem. Concr. Res., 149 (2021).
704 [52] J. Wang, E. Liu, L. Li, Multiscale investigations on hydration mechanisms in seawater OPC paste,
705 Constr. Build. Mater., 191 (2018) 891-903.
706 [53] T. Nishida, N. Otsuki, H. Ohara, Z.M. Garba-Say, T. Nagata, Some Considerations for Applicability
707 of Seawater as Mixing Water in Concrete, J. Mater. Civ. Eng., 27 (2015) B4014004.
708 [54] F. Shaheen, B. Pradhan, Influence of sulfate ion and associated cation type on steel reinforcement
709 corrosion in concrete powder aqueous solution in the presence of chloride ions, Cem. Concr. Res., 91
710 (2017) 73-86.
711 [55] T.-P. Cheng, J.-T. Lee, W.-T. Tsai, Corrosion of reinforcements in artificial sea water and
712 concentrated sulfate solution, Cem. Concr. Res., 20 (1990) 243-252.

[56] S.M. Abd El Haleem, S. Abd El Wanees, A. Bahgat, Environmental factors affecting the corrosion behaviour of reinforcing steel. V. Role of chloride and sulphate ions in the corrosion of reinforcing steel in saturated Ca(OH)2 solutions, Corros. Sci., 75 (2013) 1-15.

[57] P. Ghods, O.B. Isgor, G. McRae, T. Miller, The effect of concrete pore solution composition on the quality of passive oxide films on black steel reinforcement, Cem. Concr. Compos., 31 (2009) 2-11.

[58] K. Thangavel, N.S. Rengaswamy, Relationship between Chloride_hydroxide Ratio and Corrosion Rate of Steel in Concrete, Cement and Concrete Composites, 20 (1998) 283-292.

[59] U. Angst, B. Elsener, C.K. Larsen, Ø. Vennesland, Critical chloride content in reinforced concrete — A review, Cem. Concr. Res., 39 (2009) 1122-1138.

[60] M. Khatibmasjedi, S. Ramanthan, P. Suraneni, A. Nanni, Shrinkage Behavior of Cementitious Mortars Mixed with Seawater, Advances in Civil Engineering Materials, 8 (2019).

[61] L. Freire, M.J. Carmezim, M.G.S. Ferreira, M.F. Montemor, The passive behaviour of AISI 316 in alkaline media and the effect of pH: A combined electrochemical and analytical study, Electrochim. Acta, 55 (2010) 6174-6181.

[62] C. Andrade, M. Keddam, X.R. Novoa, M.C. Perez, C.M. Rangel, H. Takenouti, Electrochemical behaviour of steel rebars in concrete: influence of environmental factors and cement chemistry, Electrochim. Acta, 46 (2001) 3905-3912.

[63] H. Zheng, J.-G. Dai, C.S. Poon, W. Li, Influence of a Superplasticizer on Initial Corrosion of Galvanized Steel Bars in Concrete Pore Solution, J. Mater. Civ. Eng., 33 (2021).

[64] D.S. Shevtsov, I.D. Zartsyn, E.S. Komarova, Relation between resistivity of concrete and corrosion rate of reinforcing bars caused by galvanic cells in the presence of chloride, Cem. Concr. Compos., 119 (2021).

[65] A. Younis, U. Ebead, P. Suraneni, A. Nanni, Fresh and hardened properties of seawater-mixed concrete, Constr. Build. Mater., 190 (2018) 276-286.

[66] Y. Cai, H. Zheng, X. Hu, J. Lu, C.S. Poon, W. Li, Comparative studies on passivation and corrosion behaviors of two types of steel bars in simulated concrete pore solution, Constr. Build. Mater., 266 (2021).

739 [67] ASTM, G59-14, Standard Test Method for Conducting Potentiodynamic Polarization Resistance
740 Measurements, ASTM International, (2014).
741 [68] I. Martínez, C. Andrade, Polarization resistance measurements of bars embedded in concrete with
742 different chloride concentrations: EIS and DC comparison, Mater. Corros., 62 (2011) 932-942.
743 [69] C. Andrade, Propagation of reinforcement corrosion: principles, testing and modelling, Mater. Struct.,
744 52 (2018).
745 [70] H. Zheng, J.G. Dai, C.S. Poon, W. Li, Influence of calcium ion in concrete pore solution on the
746 passivation of galvanized steel bars, Cem. Concr. Res., 108 (2018) 46-58.
747 [71] A. Poursaee, C.M. Hansson, Reinforcing steel passivation in mortar and pore solution, Cem. Concr.
748 Res., 37 (2007) 1127-1133.
749 [72] G.Y. Koga, B. Albert, V. Roche, R.P. Nogueira, On the intrinsic passivating ability of Belite-
750 Ye'elimite-Ferrite towards carbon steel: A straightforward comparison, Corros. Sci., 147 (2019) 141-151.
751 [73] J. Williamson, O.B. Isgor, The effect of simulated concrete pore solution composition and chlorides
752 on the electronic properties of passive films on carbon steel rebar, Corros. Sci., 106 (2016) 82-95.
753 [74] S.M. Abd El Haleem, E.E. Abd El Aal, S. Abd El Wanees, A. Diab, Environmental factors affecting
754 the corrosion behaviour of reinforcing steel: I. The early stage of passive film formation in $Ca(OH)_2$
755 solutions, Corros. Sci., 52 (2010) 3875-3882.
756 [75] ASTM C876-15, Standard Test Method for Corrosion Potentials of Uncoated Reinforcing Steel in
757 Concrete, ASTM International, (2015).
758 [76] M. Stefanoni, U. Angst, B. Elsener, The mechanism controlling corrosion of steel in carbonated
759 cementitious materials in wetting and drying exposure, Cem. Concr. Compos., 113 (2020).
760 [77] P. Ghoddousi, M. Haghtalab, A.A. Shirzadi Javid, Experimental and numerical analysis of the effects
761 of different repair mortars on the controlling factors of macro-cell corrosion in concrete patch repair, Cem.
762 Concr. Compos., 121 (2021).

763 [78] P. Ghods, O.B. Isgor, J.R. Brown, F. Bensebaa, D. Kingston, XPS depth profiling study on the
764 passive oxide film of carbon steel in saturated calcium hydroxide solution and the effect of chloride on
765 the film properties, Appl. Surf. Sci., 257 (2011) 4669-4677.
766 [79] P. Ghods, O. Burkan Isgor, F. Bensebaa, D. Kingston, Angle-resolved XPS study of carbon steel
767 passivity and chloride-induced depassivation in simulated concrete pore solution, Corros. Sci., 58 (2012)
768 159-167.
769 [80] A. Castel, T. Vidal, R. Francois, G. Arliguie, Influence of steel–concrete interface quality on
770 reinforcement corrosion induced by chlorides, Magazine of Concrete Research, 55 (2003) 151-159.

771